

First observations of a geomagnetic superstorm with a sub-L1 monitor

E. Weiler^{1,2}, C. Möstl¹, E. E. Davies¹, A. M. Veronig^{2,3}, U. V. Amerstorfer¹,
T. Amerstorfer¹, J. Le Louédec¹, M. Bauer^{1,2}, N. Lugaz⁵, V. Haberle⁴, H. T.
Rüdissler^{1,2}, S. Majumdar¹, M. Reiss⁶

¹Austrian Space Weather Office, GeoSphere Austria, Reininghausstraße 3, Graz, 8020, Austria

²Institute of Physics, University of Graz, Universitätsplatz 5, Graz, 8010, Austria

³Kanzelhöhe Observatory for Solar and Environmental Research, University of Graz, Kanzelhöhe 19,
Treffen am Ossiacher See, 9521, Austria

⁴Conrad Observatory, GeoSphere Austria, Hohe Warte 38, Vienna, 1190, Austria

⁵Space Science Center and Department of Physics and Astronomy, University of New Hampshire, 8
College Rd, Durham, NH 03824, USA

⁶Community Coordinated Modeling Center, NASA Goddard Space Flight Center, 8800 Greenbelt Rd.,
Greenbelt, MD 20771, USA

Key Points:

- The strongest geomagnetic storm since 2003 occurred on 10–12 May 2024 and provided a unique test case for future space weather missions.
- We discuss the solar sources and interplanetary evolution of five interacting coronal mass ejections that caused this event.
- Data from STEREO-A at a sub-L1 position extended the lead time and provided a fairly accurate prediction of the geomagnetic storm magnitude.

arXiv:2411.12490v1 [physics.space-ph] 19 Nov 2024

Corresponding author: Eva Weiler, eva.weiler@geosphere.at

Abstract

Forecasting the geomagnetic effects of solar coronal mass ejections (CMEs) is currently an unsolved problem. CMEs, responsible for the largest values of the north-south component of the interplanetary magnetic field, are the key driver of intense and extreme geomagnetic activity. Observations of southward interplanetary magnetic fields are currently only accessible through in situ measurements by spacecraft in the solar wind. On 10–12 May 2024, the strongest geomagnetic storm since 2003 took place, caused by five interacting CMEs. We clarify the relationship between the CMEs, their solar source regions, and the resulting signatures at the Sun–Earth L1 point observed by the ACE spacecraft at 1.00 AU. The STEREO-A spacecraft was situated at 0.956 AU and 12.6° west of Earth during the event, serving as a fortuitous sub-L1 monitor providing interplanetary magnetic field measurements of the solar wind. We demonstrate an extension of the prediction lead time, as the shock was observed 2.57 hours earlier at STEREO-A than at L1, consistent with the measured shock speed at L1, 710 km s^{-1} , and the radial distance of 0.04 AU. By deriving the geomagnetic indices based on the STEREO-A beacon data, we show that the strength of the geomagnetic storm would have been decently forecasted, with the modeled minimum $\text{SYM-H} = -478.5 \text{ nT}$, underestimating the observed minimum by only 8%. Our study sets an unprecedented benchmark for future mission design using upstream monitoring for space weather prediction.

Plain Language Summary

Severe space weather, caused by geoeffective solar storms, has been recognized as a natural hazard. Studies have shown that extreme geomagnetic storms, occurring up to once every 50 to 100 years, may disrupt technological systems. However, predicting the effects of these solar storms is difficult. The necessary information about the storm’s internal magnetic field near Earth can currently only be collected by spacecraft at a specific point in space called L1, which is 0.01 AU in front of Earth and provides only 10 to 60 minutes warning time. In May 2024, the strongest geomagnetic storm since 2003 occurred, caused by five interacting solar storms. This study examines the solar origin of these storms and their relation to the data collected by the ACE spacecraft at L1. We also use data from another spacecraft, STEREO-A, which was slightly closer to the Sun than L1 during the event. By analyzing the STEREO-A data, we show that the strength of the storm could have been predicted fairly accurately 2 hours and 34 minutes earlier than with data just from L1. Our study provides a new standard for planning future missions using spacecraft at distances closer to the Sun than L1 to predict space weather.

1 Introduction

Coronal mass ejections (CMEs) are huge bursts of plasma from the Sun and the main cause of severe space weather phenomena at Earth. However, not every CME directed towards the Earth is geoeffective (e.g. Kilpua et al., 2019; Temmer et al., 2023). Whether CMEs that hit the Earth cause a geomagnetic storm depends on the orientation of the magnetic field embedded in the CME. Specifically, it matters whether the magnetic field component parallel to the Earth’s magnetic axis is directed southward. In that case, magnetic reconnection with the oppositely directed Earth magnetic field can occur. Although we can draw conclusions about the structure and propagation of CMEs in the heliosphere from remote sensing, the prediction of the southward magnetic field component is still an unsolved problem in space weather research, known as the B_z problem (e.g. Vourlidas et al., 2019).

The geomagnetic impact of CMEs is generally quantified via geomagnetic indices, one of the most widely used being the disturbance storm time (Dst) index, measured in nanotesla (nT) and provided by the World Data Center for Geomagnetism, Kyoto (Sugiura, 1964; Nose et al., 2015). This measure has been available since 1957, and thus, is well

suiting for comparison with historic storms. The Dst index quantifies the reduction of the horizontal magnetic field on the ground due to the enhancement of the magnetospheric ring current and is calculated every hour from four mid-latitude ground observatories. It is used to characterize the strength of geomagnetic storms, with minimum Dst indices of less than -50, -100, -200, and -250 nT indicating moderate, severe, intense, and superstorms, respectively (e.g. Collado Villaverde et al., 2023). CMEs are the exclusive driver for intense events (e.g. Zhang et al., 2007), with successive and possibly interacting CMEs thought to be the cause of the most severe storms (e.g. Liu et al., 2014; Meng et al., 2019; Koehn et al., 2022). Geomagnetic superstorms can cause damage to satellites, power grids and disrupt communications, making the development of appropriate forecasting and mitigation measures a necessity for our technology-dependent society.

Currently, we rely mainly on in situ observations from spacecraft positioned at the first Lagrangian Point (L1), located 0.01 AU upstream (sunward) of Earth, to obtain reliable estimates of the severity of geomagnetic storms. Some of these spacecraft, namely the Advanced Composition Explorer (ACE; Stone et al., 1998) and the NOAA-operated Deep Space Climate Observatory (DSCOVR; Burt & Smith, 2012), transmit interplanetary magnetic field and plasma data in real-time, with a delay of only a few minutes, allowing us to predict the geomagnetic effects of CMEs 10 to 60 minutes before the CME reaches Earth.

Burton et al. (1975) was the first to find an empirical relationship to forecast the ground-based Dst index, and thus the strength of the geomagnetic storm, using the measured interplanetary magnetic field and plasma parameters. Since then, many others have worked on creating solar wind-to- Dst index models, ranging from empirical and semi-empirical to machine learning modeling approaches (e.g. O'Brien & McPherron, 2000). Ji et al. (2012) found that the Temerin and Li (2006) model (henceforth referred to as the TL model) achieved the best prediction performance for severe geomagnetic events out of 63 different models. This model is semi-empirical and was optimized using eight years of solar wind data, achieving a root mean square error (RMSE) of 6.65 nT between the observed and predicted Dst index.

On 10–12 May 2024, the strongest geomagnetic storm since 2003 took place, with a minimum Dst of -412 nT, which is thought to be around 30–50% the magnitude of the most extreme events (e.g. Riley, 2012; Love et al., 2015, 2024). Consequentially, problems with the positioning global navigation satellite systems, the drop in orbital height of satellites, the rerouting of flights, and strong geoelectric fields have been reported, but no major damages nor unplanned outages of power grids were observed (e.g. Hayakawa et al., 2024; Spogli et al., 2024; Themens et al., 2024). Mitigation measures for geomagnetically induced currents have been reported, for example, in the USA and New Zealand, with the relevant guidelines for New Zealand given in Mac Manus et al. (2023). On the bright side, for tens, if not hundreds of millions of people, the chain of events presented the first time to experience the northern and southern lights as the auroral oval expanded to lower latitudes.

As the superstorm was measured not only by spacecraft at L1 (at 1.00 AU), but also by the Solar TERrestrial RELations Observatory (STEREO-A; Kaiser et al., 2008) positioned at 0.96 AU and 12.6° west of Earth (located at 1.01 AU), this event gives us the first opportunity to study how a spacecraft situated closer to the Sun than L1 could improve both the lead time and accuracy for forecasting the geomagnetic effects of superstorms. This is particularly interesting with regard to future mission concepts for sub-L1 monitors, which are intended to improve the predictability of space weather by deploying spacecraft further upstream than L1 (e.g. Lindsay et al., 1999; Cyr et al., 2000; Kubicka et al., 2016; Morley, 2020; Laker et al., 2024; Lugaz, Lee, et al., 2024).

Depending on the location of the sub-L1 monitor, the warning time for large-scale disturbances in the solar wind, including CMEs but also high-speed streams, could be

extended by several hours. Various strategies have been proposed to achieve this goal, in particular the stationing of preferably multiple spacecraft on distant retrograde orbits (DROs; Henon, 1969; Cyr et al., 2000; Borovsky, 2018), on a Venus-like orbit (Ritter et al., 2015), or the placement of a spacecraft around imaginary Lagrange points using solar sails (Lindsay et al., 1999; Eastwood et al., 2015). The spacecraft for such missions must naturally lie in the ecliptic plane and must not deviate too much from the Sun-Earth line in order to ensure a certain degree of accuracy, regarding the longitudinal coherence of CMEs and processes that influence CME propagation. The ideal orbital distance of these spacecraft has not yet been determined, as there is a lack of multi-spacecraft observations of CMEs at medium separations (1° to 20° in heliospheric longitude). However, recent studies (e.g. Good & Forsyth, 2016; Lugaz, Zhuang, et al., 2024) have shown that the longitudinal separation between two spacecraft should be less than 15° to ensure that most CME magnetic ejecta are actually measured at both spacecraft. Since STEREO-A has a longitudinal separation of 12.6° , the May 2024 event is considered to be in the upper longitudinal separation range for which monitoring at distances closer to the Sun than L1 is still feasible. As it is the first event that led to a geomagnetic superstorm being observed by a sub-L1 monitor, it provides a unique opportunity to test the real-time predictive capability of superstorms from a sub-L1 perspective. To this end, our analysis simulates a real-time scenario when modeling the geomagnetic effects from STEREO-A data, using only data and knowledge available at the time of the event.

In this study, we examine the origin of the CMEs that caused the May event and their propagation in remote images, connecting these to in situ observations at both STEREO-A and L1, and compare the predicted and observed geomagnetic effects. The first three sections give a chronological summary of the event. We start with an analysis of the source region and describe the remote sensing data used for our study and the derivations thereof in section 2. In section 3 we simulate the propagation of the CMEs in the heliosphere using the semi-empirical propagation tool ELEvo. The in situ magnetic structures of the CMEs as measured by STEREO-A and ACE are analyzed in section 4, where we link those to their solar and interplanetary counterparts, as inferred from solar and heliospheric observations, respectively. We explain the TL model and the processing of the STEREO-A beacon data in section 5. The resulting modeled geomagnetic indices from real-time STEREO-A and L1 data as well as a comparison to observed indices are presented in the same section. Finally, in section 6 our results and main findings are summarized and discussed.

2 Solar and Remote Sensing Observations

To study the source regions of these CMEs we use different filters of the Solar Dynamics Observatory (SDO; Pesnell et al., 2012) Atmospheric Imaging Assembly (AIA; Lemen et al., 2012) as well as the Helioseismic and Magnetic Imager (HMI; Scherrer et al., 2012). Furthermore, we use $H\alpha$ observations from the Cerro Tololo observatory in Chile, which is one of six telescopes of the Global Oscillation Network Group (GONG; Harvey et al., 1996).

Figure 1 shows the active region AR 13664. Four of the five CMEs (numbers 1, 2, 4, and 5) that caused the main geomagnetic effect on 10–11 May 2024 originated from this solar active region and were associated with major flares of soft X-ray class X1.0, M8.3, X1.0/M9.8 (double peak), and X2.2 (see Table 1), whereas CME 3 originated from a different region on the Sun. During 8–9 May 2024, AR 13664 was located close to disk center (20° S, 10 – 20° W), was of complex magnetic type ($\beta\gamma\delta$), and covered a size as large as about 1200 micro-hemispheres. Starting from 7 May 2024, it showed a steep increase in its free magnetic energy, with a value of about $1 \cdot 10^{33}$ erg on 8 May 2024 (Jarolim et al., 2024; Hayakawa et al., 2024). The flares related to CMEs 1 and 2 occurred in the eastern (trailing) part of the elongated AR 13664; the flares associated with CMEs 4 and 5 also had their center in the AR’s trailing segment, but in addition also revealed flare

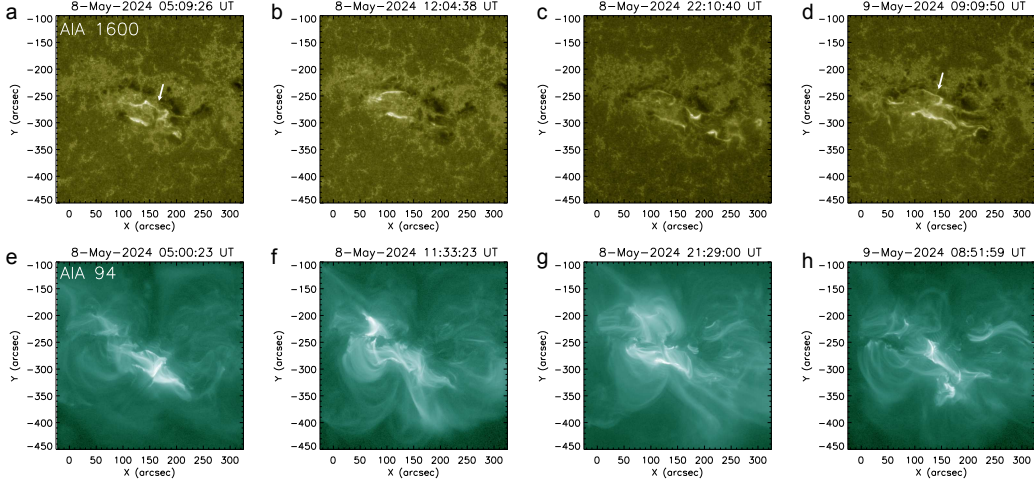


Figure 1. Snapshots of the four events from AR 13664 from SDO/AIA 1600 Å and 94 Å filtergrams, (a)–(d) imaging the flare ribbons in the chromosphere and (e)–(h) the hot flaring corona (at a temperature of ~ 7 MK). All images are differentially rotated to 8 May 2024, 05:00 UT. The white arrows in (a) and (d) highlight forward J-shaped flare ribbons.

ribbons extending to its western segment. Each of these four CMEs were associated with impulsive hot loop eruptions observed by the 94 and 131 Å filters (Figure 1e–h), which have peak formation temperatures of ~ 7 and 10 MK, respectively. From the 94 Å filter, we can also infer that the direction of these eruptions was toward the south-west for CMEs 1 and 4, and to the south for CMEs 2 and 5. As one can see from Figure 1a–d, for all four events that originated from AR 13664, the flare ribbons (and the associated magnetic polarity inversion line (PIL) between them) have a low inclination (about 20° with respect to the solar equator). Considering several solar proxies, such as the flare ribbons (e.g. forward J-shape in Figure 1a and d), the left-skew of overlying coronal loops (Figure 2a) and of post-eruptive flare arcades (Figure 2b), one would expect right-handed, low inclination, and hence south-west-north (SWN) flux ropes in situ, with the axial field direction pointing westward for all eruptive CMEs. Information about different solar proxies can be found in e.g. Palmerio et al. (2017), and the definition of the flux rope types is given in Bothmer and Schwenn (1998).

CME 3 originated from a quiet-Sun filament eruption located to the south of AR 13667 and of the northern polar coronal hole, with its center around (-25°E , 20°N). The filament is visible in H α observations of the GONG observatory in Cerro Tololo (Figure 2a). The extended erupting filament that caused CME 3 is associated with a distinct dimming (see Figure 2d), with its northern segment extending to the polar coronal hole. The location of this dimming and the right-skewed flare arcades connecting the dimming regions indicate a dextral filament which corresponds to a negative magnetic helicity (Martin, 1998; Chen et al., 2014). The solar proxies would hence indicate a south-east-north (SEN) flux rope for CME 3 in situ.

Panels a–d of Figure 3 show the five CMEs as observed with the Large Angle Spectroscopic Coronagraph (LASCO; Brueckner et al., 1995) on board the Solar and Heliospheric Observatory (SOHO; Domingo et al., 1995). The different CMEs are visible as halo CMEs and can be clearly identified separately. The first eruption enters the field of view (FOV) of LASCO/C2 on 8 May 2024, 05:36 UT (see also Table 1) and shows an increased brightness in a south-westerly direction. The second eruption is weaker than the first, but the front is still clearly distinguishable and appears for the first time at 12:24 UT

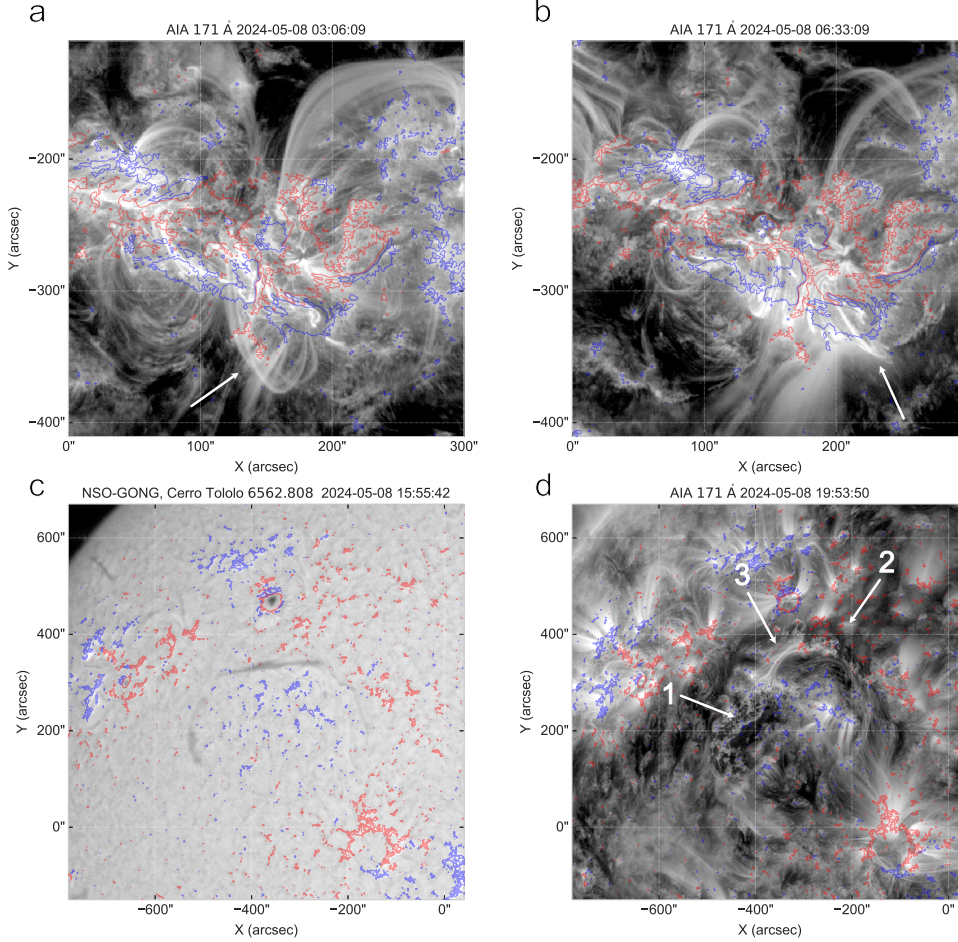


Figure 2. Solar proxies to derive magnetic helicity. (a)–(b) AR 13664 in the southern hemisphere observed in the AIA 171 Å filter, with the arrow in (a) showing the overlying coronal loops, and the arrow in (b) showing the flare arcades. (c) Filament in northern hemisphere as observed in H α by GONG, Cerro Tololo observatory. (d) Dimming region (arrows 1 and 2) and skew of post-eruptive arcades (arrow 3) as seen in the AIA 171 Å filter. The snapshots are overlaid with HMI magnetograms saturated at ± 100 G (a)–(b) and ± 300 G (c)–(d). Red colors indicate positive polarity, blue colors negative polarity.

in the LASCO/C2 FOV. Figure 3c shows CME 3 and CME 4: While the filament eruption from AR 13667 moves in a north-easterly direction, CME 4, which enters the field of view 3.37 hours later, propagates in a south-westerly direction. CME 5 is again visible as a halo CME starting on 9 May 2024, 09:24 UT (Figure 3d).

Figure 3e displays the resulting Jplot from observations of the Heliospheric Imagers (HI; Eyles et al., 2009) onboard STEREO-A that allow us to follow the propagation of the CMEs through the inner heliosphere. We identify the different fronts of the CMEs as indicated by the different colors, which also match the colored labels in Figures 3a–d. We conclude that CME 3 is overtaken by CME 4 shortly after both enter the field of view of HI1. However, it is unclear whether the two CMEs physically interact. HI1 provides line-of-sight observations that could lead to an apparent overlap of these CMEs

Table 1. Flare parameters associated with the five CMEs that erupted on 8–9 May 2024. CME 3 is not linked to a flare, the peak flare time corresponds to the start of the filament eruption. CME 4 is associated with a double-peaked flare.

CME	1st obs. in LASCO/C2	flare	source region	peak flare time
1	2024-05-08T05:36Z	X1.0	S22W10 (13664)	2024-05-08T05:09Z
2	2024-05-08T12:24Z	M8.6	S20W11 (13664)	2024-05-08T12:04Z
3	2024-05-08T19:12Z	-	N26E22 (13667)	2024-05-08T08:15Z
4	2024-05-08T22:24Z	X1.0	S20W17 (13664)	2024-05-08T21:40Z
		M9.8	S22W22 (13664)	2024-05-08T22:27Z
5	2024-05-09T09:24Z	X2.2	S20W25 (13664)	2024-05-09T09:13Z

in the images, but this need not be the case in 3D. Also, the longitudinal distance between the apices of CME 3 and CME 4 is quite large and amounts to 29° .

3 CME Arrival Time and Speed Modeling

Figure 4 shows a snapshot of the ELLiptical Evolution model (ELEvo; Möstl et al., 2015) visualizing the propagation of the five CMEs through the heliosphere.

The ELEvo model assumes an elliptical front for the CMEs and includes a simple drag-based model (Vršnak et al., 2013). The snapshot is taken at the time of the measured arrival of the first CME at L1 on 8 May 2024 at 16:37 UT. On the left panel, a top-down view of the heliosphere with the different spacecraft and planet positions is presented in Heliocentric Earth Equatorial (HEEQ) coordinates. Real-time STEREO-A beacon and ACE data are shown on the right. The first panel shows the speed data from ACE. The second and third panels display the magnetic field data in Geocentric Solar Magnetospheric (GSM) coordinates from ACE and STEREO-A, respectively. Here we will discuss the simulation of the five CMEs with ELEvo, a detailed discussion of the in situ data follows in section 4.

The CME parameters required as input for the ELEvo model, initial time at $21.5 R_\odot$, initial speed and direction of the CME, are taken from the Space Weather Database of Notifications, Knowledge, Information (DONKI; <https://kauai.ccmc.gsfc.nasa.gov/DONKI/>) provided by the Moon to Mars (M2M) Space Weather Analysis Office and hosted by the Community Coordinated Modeling Center (CCMC; <https://ccmc.gsfc.nasa.gov/>). As can be seen, ELEvo reproduces the actual arrival time of CME 1 at L1 well. The time difference between the calculated and the observed arrival time is only ~ 2 min, with a model error window of ± 7 hours. The model error results from including 50,000 ensemble members with slightly different initial parameters, randomly varied along a normal distribution, in the ELEvo runs (see also Čalogović et al., 2021). Atop the first in situ panel, we plot the normal distributions of the arrival time at L1 resulting from the ensemble for each CME. The shaded area around the ellipses on the left, simulating the shock fronts, shows the corresponding $\pm 1\sigma$ uncertainty. In the speed panel, we also indicate the estimated arrival speed of the CMEs at L1, whereby the arrival speed is underestimated for CMEs 1, 2, and 3 and overestimated for CMEs 4 and 5. At 889 km s^{-1} , the arrival speed of CME 5, which is modeled to be the third to arrive at Earth, deviates the most from the actual measured speed of $\sim 700 \text{ km s}^{-1}$ at the predicted arrival time of CME 5. Although the ELEvo model predicts the arrival of the first CME at L1 accurately, it forecasts the arrival of the same CME at STEREO-A (see third panel) 1 h 34 min too early, which is, however, still a good prediction.

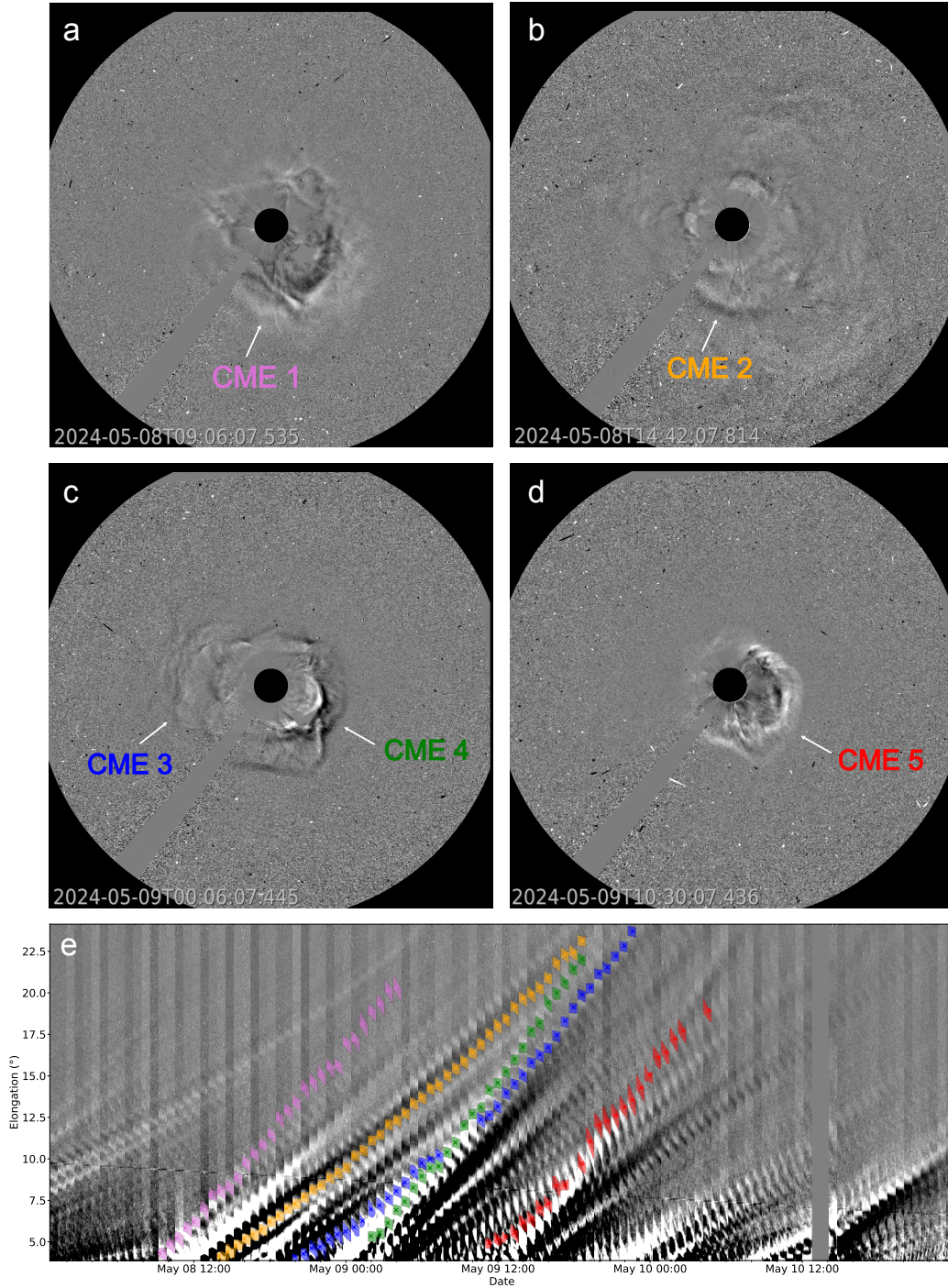


Figure 3. Interplanetary evolution of the five CMEs that caused the superstorm on 10–11 May 2024. (a)–(d) LASCO/C2 and C3 observations of the five halo CMEs with white arrows indicating the different fronts, (e) fronts of the different CMEs tracked in STEREO-A/HI1 running differences highlighted in the corresponding Jplot cut around the ecliptic.

The simulation shows that the apex direction of the CMEs originating from the southern hemisphere is slightly west of the Sun-Earth line. In particular, CME 1 with

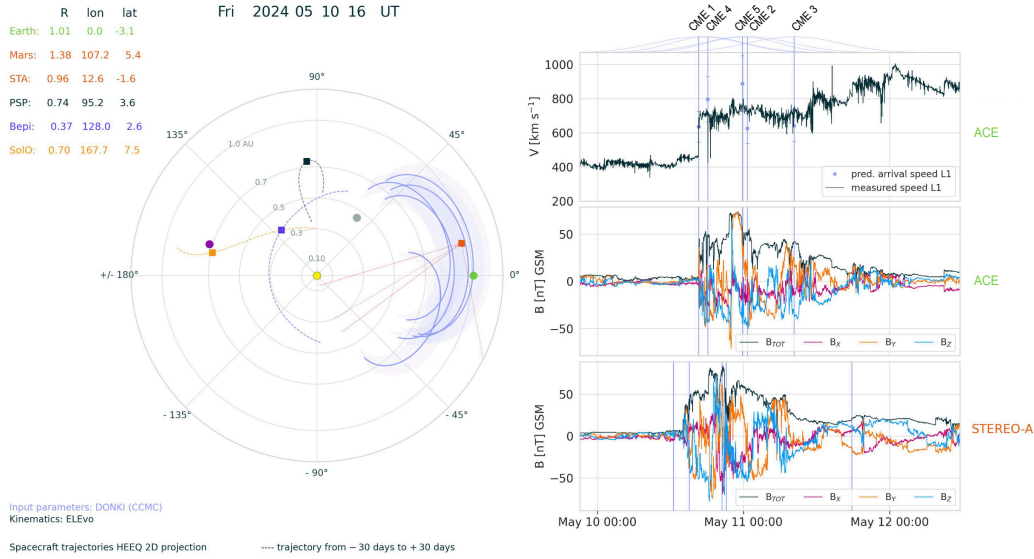


Figure 4. Snapshot of the ELEvo model at 10 May 2024, 16:00 UT. Left: A view of the heliosphere from above with the different spacecraft positions of STEREO-A (red), Solar Orbiter (SolO; orange), Parker Solar Probe (PSP; black), BepiColombo (Bepi; blue), and L1 (green) displayed in Heliocentric Earth Equatorial (HEEQ) coordinates. The propagation of the five different CMEs is shown, assuming an elliptical front, with the shaded areas indicating the $\pm 1\sigma$ uncertainties of the arrival time. Right: In situ speed and magnetic field data from ACE in real-time, and STEREO-A real-time beacon data. The vertical blue lines indicate the predicted arrival times at L1 as issued by ELEvo. The blue dots in the first panel correspond to the predicted arrival velocities at L1, with the error bars indicating the $\pm 1\sigma$ uncertainty. Input parameters for the CMEs are taken from the DONKI database (CCMC).

an inferred apex direction of 12° appears to be heading towards STEREO-A head-on. The filament eruption from the northern hemisphere (i.e. CME 3), in contrast, is moving more to the east and is the last to reach Earth, according to ELEvo. This is not necessarily the case for the actual propagation, as the propagation model is not able to reproduce the interaction of the different CMEs. However, even by simply propagating the individual CMEs outwards, the simulation suggests that all five CMEs would arrive within 15.5 hours of each other at L1, which already hints at a rather complex in situ signature there.

4 In situ Spacecraft Observations

To study the in situ measurements of the five CMEs, we inspect real-time data from the ACE spacecraft, positioned at L1 (at 1.00 AU), and the STEREO-A spacecraft (at 0.96 AU) acting as a sub-L1 monitor. We use the ACE Magnetic Field Experiment (MAG; Smith et al., 1998) and the Solar Wind Electron Proton Alpha Monitor (SWEPAM; McComas et al., 1998) for real-time measurements of the local (i.e. L1) magnetic field and solar wind plasma, respectively. The magnetometer instrument IMPACT (Acuña et al., 2008) onboard STEREO-A is used for measurements of the magnetic field at the STEREO-A position (i.e. sub-L1). For our analysis we use STEREO-A beacon data, which is produced in real-time.

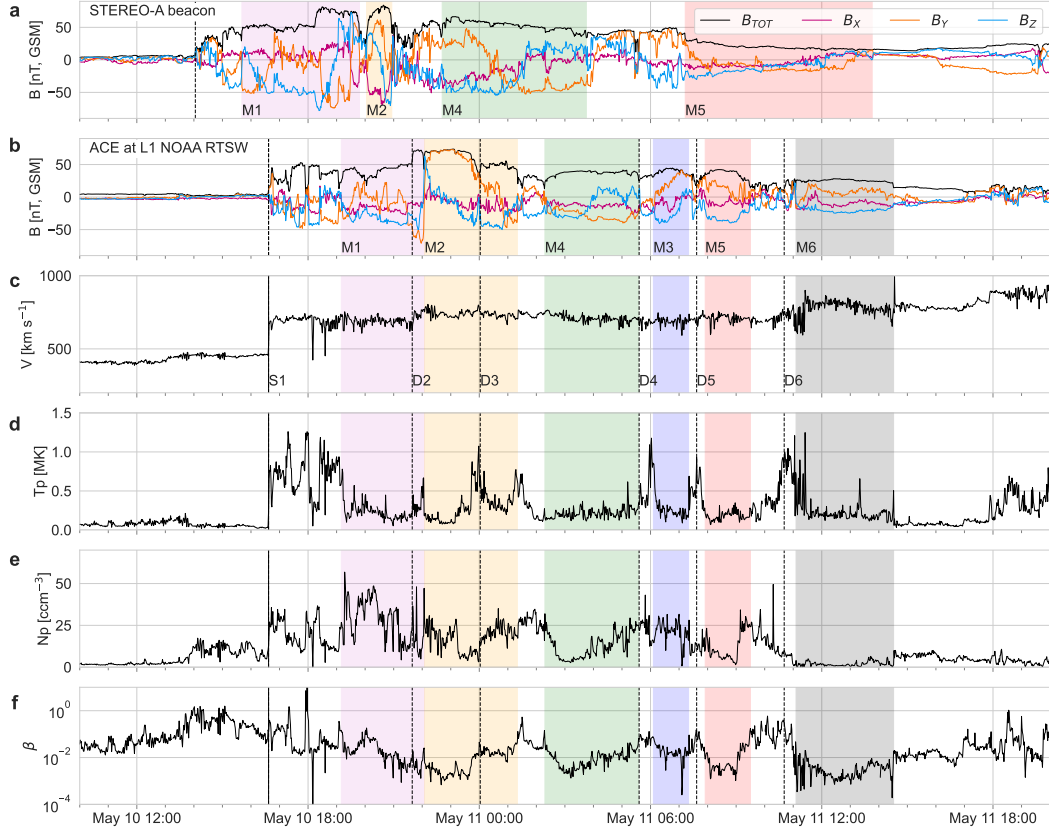


Figure 5. In situ measurements of the complex CME-CME interactions at L1 and STEREO-A. (a) The magnetic field vector observed in real-time by STEREO-A/IMPACT, located at 12.6° longitude west of Earth, with identified magnetic obstacles indicated as shaded regions and named M1, M2, M4, and M5. The first shock arrival time (10 May 2024 14:03 UT) is marked as a dashed line. (b), NOAA real-time solar wind magnetic field vector, provided by the magnetometer ACE/MAG. Identified magnetic obstacles are named M1–M6 and indicated by the corresponding shaded regions. The start times for each CME are given as dashed lines. (c) Plasma speed measured by ACE/SWEPAM. (d) Observations of the plasma proton temperature T_p observed by the ACE/SWEPAM instrument. Enhancements of T_p that we link to the individual CME arrivals are marked as vertical dashed lines named S1 for the initial shock, and then D2–D5 for discontinuities that mark the CME start times. (e) Solar wind plasma proton density N_p , and (f) plasma β , ratio of plasma to magnetic pressure, both from ACE/SWEPAM.

Figure 5a shows the magnetic field data observed by STEREO-A IMPACT, where an interplanetary shock starts at 14:03 UT on 10 May 2024. The shock is preceded by a period of undisturbed solar wind conditions. Figures 5b–f show the magnetic field and plasma data measured by the ACE spacecraft at L1. In the magnetic field data of Figure 5b, an interplanetary shock starts on 10 May 2024 16:37 UT, 2 h 34 min after the shock was measured at STEREO-A. After the shock, six magnetic ejecta can be identified (M1–M6), which have interacted but not yet merged and can therefore still be individually distinguished. The identification of the different magnetic ejecta regions is mainly performed by focusing on rotations of the magnetic field vector and low plasma beta values (see Figure 5f). Due to the successive launch of the CMEs within 28 hours, the expansion of the individual CMEs is inhibited, leading to a preservation of high magnetic

field strengths at L1, with a maximum of 74.8 nT on 10 May 2024, 23:05 UT. This is consistent with previous simulations of CME-CME interaction (e.g. Lugaz et al., 2005; Scolini et al., 2020). Furthermore, the lack of expansion leads to a short duration of all ME, ranging from only 1h 14min for M3 to 3h 35min for M6.

Table 2. Positions of ACE and STEREO-A at shock arrival time in HEEQ coordinates, and arrival times of the shock and start and end times of the magnetic obstacles (UT) of the identified CMEs.

Spacecraft	shock arrival [UT]	R [au]	lon [deg]	lat [deg]
ACE	2024-05-10 16:37	1.000	-0.013	-3.072
STEREO-A	2024-05-10 14:03	0.956	12.554	-1.570

Spacecraft	CME	ICME start [UT]	MO start [UT]	MO end [UT]
ACE	1	2024-05-10 16:37	2024-05-10 19:10	2024-05-10 22:04
ACE	2	2024-05-10 21:38	2024-05-10 22:05	2024-05-11 01:20
ACE	3	2024-05-11 05:36	2024-05-11 06:06	2024-05-11 07:20
ACE	4	2024-05-11 00:02	2024-05-11 02:18	2024-05-11 05:35
ACE	5	2024-05-11 07:37	2024-05-11 07:55	2024-05-11 09:30
ACE	6	2024-05-11 10:41	2024-05-11 11:06	2024-05-11 14:31
STEREO-A	1	2024-05-10 14:03	2024-05-10 15:41	2024-05-10 19:48
STEREO-A	2	2024-05-10 18:14	2024-05-10 20:03	2024-05-10 20:56
STEREO-A	4	2024-05-10 21:41	2024-05-10 22:42	2024-05-11 03:45
STEREO-A	5	2024-05-11 05:36	2024-05-11 07:13	2024-05-11 13:46

Table 2 presents the corresponding times of the identified magnetic obstacles of the five magnetic ejecta (M1-M5), discussed in detail, as well as another magnetic flux rope (M6), which does not contribute as much to the geomagnetic response. Four out of the six ejecta identified in the ACE data are also identified in the STEREO-A data. More specifically, the similar rotational behavior of the flux ropes leads to the conclusion that M1, M2, M4 and M5 in the ACE data match the four identified ejecta in the STEREO-A data (as indicated by the colored shading). The ejecta identified in both STEREO-A and L1 data are right handed, with M2 and M4 classified as north-east-south (NES) and SWN flux rope types, respectively. The flux rope type of M1 is hard to determine from in situ data alone, however, when applying the 3D coronal rope ejection model (3DCORE) to the ACE data, the model indicates an east-south-west (ESW) flux rope type (see Figure 6) as well as a right-handed, high inclination flux rope. The 3DCORE model assumes a Gold-Hoyle-like flux rope with an elliptical cross-section that stays attached to the Sun at all times. The tapered torus expands self-similarly and propagates through the heliosphere according to a drag-based model. Detailed information about 3DCORE can be found in Weiss, Möstl, Amerstorfer, et al. (2021) and Weiss, Möstl, Davies, et al. (2021).

Looking again at the source region, one would expect the CMEs emanating from AR 13664 to have a SWN flux rope in situ (see section 2). This, however, is only valid for M4. M3 in the ACE data is the only flux rope that shows a left-handed helicity. More specifically, the flux rope type of M3 is SEN, which is consistent with the flux rope type inferred from solar proxies of AR 13667 in the northern hemisphere. This leads us to the conclusion that M3 corresponds to CME 3 associated with the filament eruption. In addition, M3 cannot be identified in the magnetic field data from STEREO-A, possibly due to the longitudinal separation of 34 degrees between AR 13667 and STEREO-A. In contrast, the in situ signatures M1, M2, M4, and M5 are most likely associated with CME 1, CME 2, CME 4, and CME 5, respectively, originating from AR 13664 in the southern hemisphere (see also Table 2). It is also noteworthy that these flux ropes show pe-

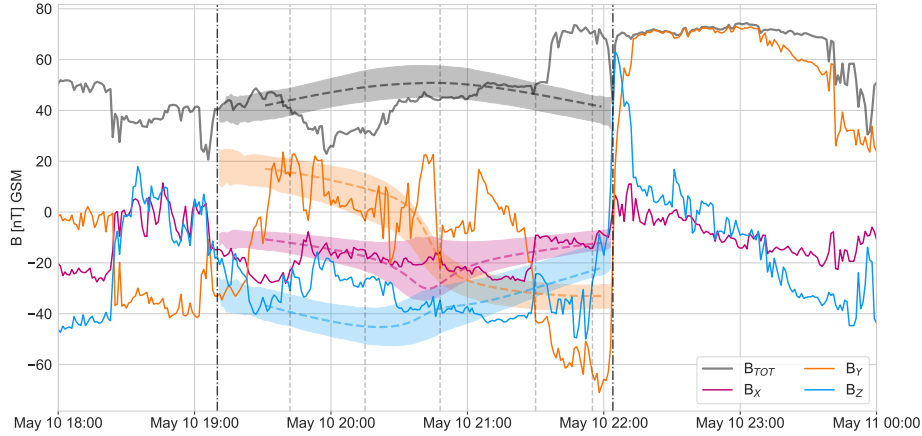


Figure 6. 3DCORE reconstruction of the M1 in situ flux rope signature observed at L1. The shaded areas correspond to the 1σ spread of the ensemble. The dashed colored lines show one specific flux rope from the ensemble. The vertical gray dashed lines delineate the fitting points at which 3DCORE evaluates the reconstruction, and the black dashed dotted lines show the start and end of the reconstruction interval. The data are presented in the GSM coordinate system.

riods of prolonged negative B_z , possibly resulting from the PIL orientation, which is tilted by 20° from the ecliptic plane, as discussed in section 2, and in more detail in Wang et al. (2024).

We also identify discontinuities in the ACE data, denoted as D2–D6 in Figure 5. We hypothesize that D2 was a shock driven by one of the overtaking CMEs and decayed into a compression wave due to the extreme magnetosonic speed $v_{ms} = 271 \text{ km s}^{-1}$ inside the magnetic ejecta of M1. Nevertheless, D2 causes a compression of the upstream magnetic field magnitude, B_{tot} , by a factor of 1.3, which also leads to an amplification of the B_z component, with a minimum of -49 nT at 21:56 UT. D3 also has weak Alfvén and magnetosonic Mach numbers of $M_a = 0.8$ and $M_{ms} = 0.7$, respectively. It causes the B_z component to drop from -2 nT to -36 nT , which remains increasingly negative for one hour. The parameters for these discontinuities as well as S1, which is a fast forward interplanetary shock, are given in Table 3. The shock/discontinuity normal is calculated using 10-min averaged up- and downstream values. For the discontinuity analysis, we use ACE science data instead of real-time data, as it provides the velocity components v_x, v_y, v_z . We can then use the velocity and magnetic field co-planarity method (Colburn & Sonett, 1966) as well as a set of three equations for the mixed mode method (Abraham-Shrauner, 1972; Abraham-Shrauner & Yun, 1976) to get five slightly different estimations of the shock/discontinuity normal. The shock speed is calculated from these estimates following Schwartz (1998). The resulting discontinuity normal varies the most for D3, which is why the uncertainty for the parameters derived thereof is large.

5 Modeling of Geomagnetic Effects

In this section, we demonstrate how a sub-L1 monitor may have been used to predict the geomagnetic effects of the May superstorm. To do this, we treat our analysis as though it was performed in real-time, meaning that we only use data and knowledge that were available during the time of the event on 10 and 11 May. As previously stated,

Table 3. Shock/discontinuity parameters for the features S1, D2 and D3. c_s , v_a , v_{ms} , correspond to sound, Alfvénic, and magnetosonic speed, respectively, M_a is the Alfvénic and M_{ms} the fast magnetosonic Mach number. The shock speed is given in the frame of the solar wind.

	S1	D2	D3
shock normal (deg)	46 ± 6	81 ± 8	30 ± 29
shock speed (km s^{-1})	684 ± 41	854 ± 243	78 ± 16
upstream v_a (km s^{-1})	267	240	226
upstream c_s (km s^{-1})	46	48	74
upstream fast v_{ms} (km s^{-1})	33	271	237
M_a	12.4 ± 0.4	1.1 ± 0.4	0.8 ± 0.7
M_{ms}	9.9 ± 0.3	1.1 ± 0.4	0.7 ± 0.6

we aim to derive geomagnetic indices, namely *Dst* and SYM-H, using STEREO-A beacon data, with SYM-H being the de facto high resolution *Dst* index (Wanliss & Showalter, 2006).

The geomagnetic effects are modeled with the TL model, which can be applied to any time resolution. When applied to data with hour and minute resolution, we compare the result with observed *Dst* and SYM-H values, respectively, taken from low and high resolution OMNI data (<https://spdf.gsfc.nasa.gov/pub/data/omni/>; Papitashvili & King, 2020b, 2020a). The TL model requires the speed, density and magnetic field components in GSM coordinates of the solar wind at L1 as input. Since STEREO-A is 0.04 AU upstream of L1, the data has to be spatially and temporally mapped to L1 before the model can be applied. In addition, the TL model depends on the local time as well as past *Dst* and magnetic field values. To initialize the model, estimates for the model parameters *Dst1*, *Dst2*, *Dst3* are needed.

Figure 7 shows the mapped STEREO-A beacon data, compared to real-time ACE data, and the resulting geomagnetic indices calculated from the shifted STEREO-A as well as the observed L1 data. How the STEREO-A data is mapped to L1 and how missing values in the STEREO-A data are estimated is explained below.

We first transform the STEREO-A beacon data, which are available in radial-tangential-normal (RTN) coordinates, to the GSM coordinate frame by successively applying Hapgood (1992) routines. The STEREO-A data are then mapped spatially and temporally to L1: Since STEREO-A is 0.04 AU closer to the Sun than L1, we expect the CMEs to expand further after being measured at STEREO-A and therefore to have a slightly lower magnetic field strength at L1. We account for this by applying a power law $B_i(r) \propto r^\alpha$, $i = x, y, z$ with $\alpha = -1.66$ (Davies et al., 2021) to the STEREO-A magnetic field components B_x , B_y , B_z . Since ELEvo already indicates a highly interactive structure at L1, we consider this expansion rate as an upper limit and also look at the case where there is no expansion at all (i.e. $\alpha = 0$). Figure 7a shows the scaled and temporally shifted STEREO-A magnetic field components.

During the event, STEREO-A beacon speed and density data were not available in real-time. We therefore use the ELEvo model to estimate the different arrival speeds of the CMEs at STEREO-A. For the duration of the event (indicated by the vertical lines in Figure 7) we set the speed to $725 \pm 118 \text{ km s}^{-1}$, which is the average of all five predicted arrival speeds at STEREO-A. This agrees well with the observed mean speed at L1 = 716 km s^{-1} during the event. The density during the event is estimated by using an average value derived from the HELIO4CAST ICMECAT catalog (Möstl et al., 2020). The mean proton density for CMEs at L1 as measured by Wind is 11.5 cm^{-3} , including both the sheath region and magnetic obstacles. The speed and density before the

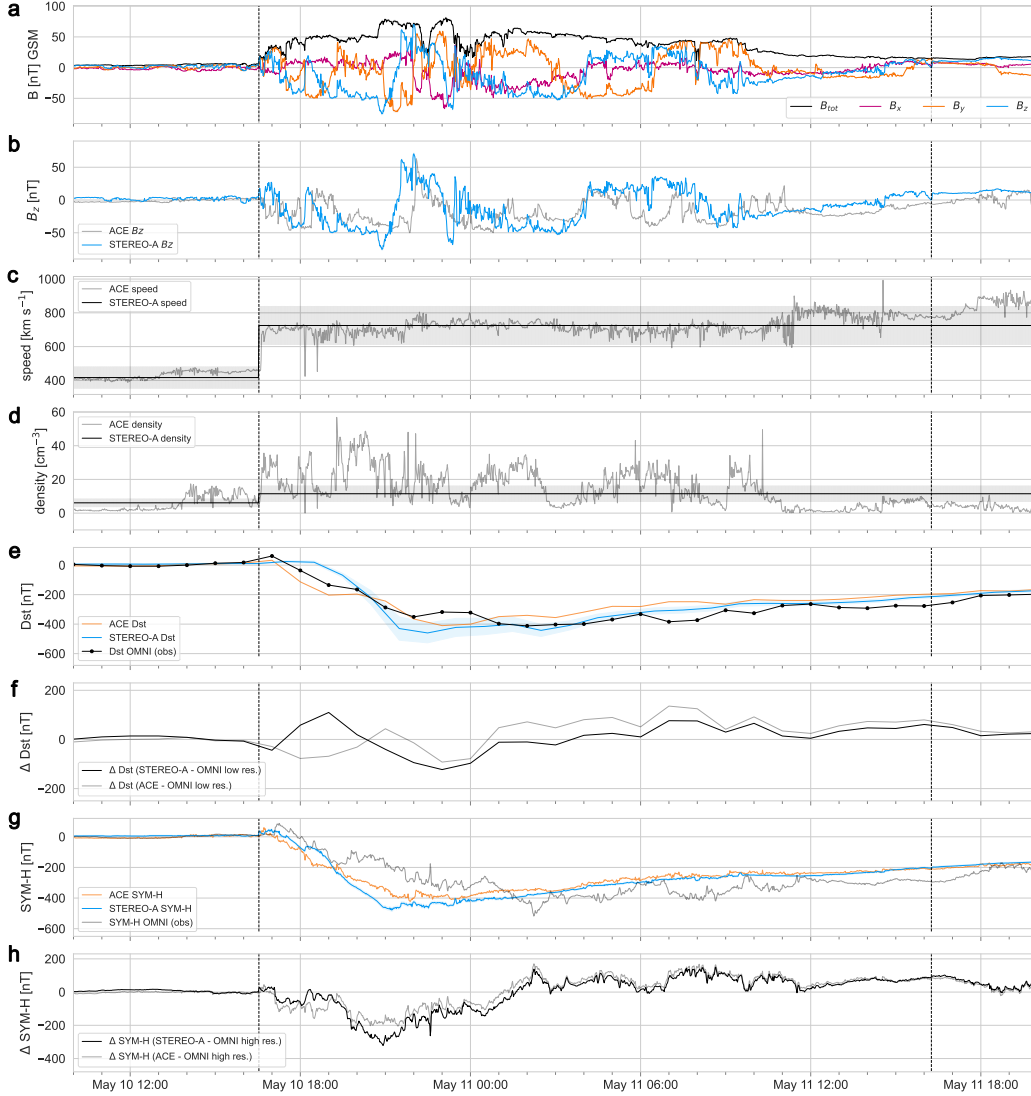


Figure 7. Modeling of the geomagnetic magnitude based on STEREO-A beacon data mapped to L1. (a) The scaled and shifted STEREO-A magnetic field components B_x , B_y , B_z , and B_{tot} in GSM coordinates, (b) shifted STEREO-A B_z component compared to the B_z component at L1, (c)-(d) estimated speed and density (black) compared to the bulk speed and density as measured by ACE at L1 (gray), (e) modeled Dst index for STEREO-A (blue) and ACE (orange) data compared to the observed Dst values as given in the low resolution OMNI dataset, (f) difference between observed and modeled Dst index from STEREO-A (L1) data in black (gray), (g) Modeled SYM-H index for STEREO-A (blue) and ACE (orange) data compared to the observed SYM-H values as given in the high resolution OMNI dataset, (h) difference between observed and modeled SYM-H from STEREO-A (L1) data in black (gray).

event are estimated by averaging the ambient solar wind conditions at L1 in a 10-hour interval before the shock arrival at STEREO-A at 10 May 14:03 UT, which results in 416 km s^{-1} and 6 cm^{-3} , respectively. Figures 7c-d show the estimated values for the speed and density at the STEREO-A position in comparison with measured speed and density values from ACE at L1.

We assume that the actual time difference between the shock measured at STEREO-A and L1 is unknown, again mimicking a real-time scenario. Instead, we estimate the arrival time using the averaged predicted arrival speed at STEREO-A, $725 \pm 118 \text{ km s}^{-1}$, and the radial distance between STEREO-A and L1, 0.04 AU. The resulting time shift of 2.5 ± 0.9 hours is then applied to the whole STEREO-A data set. With the actual time difference being 2.57 hours, we introduce an error of ~ 5 min to the geomagnetic index forecast. To differentiate between modeling and observational effects, we also calculate the geomagnetic indices using the observed L1 solar wind data and compare both results with the observed SYM-H and *Dst* values.

To account for the error we make in shifting the data to L1, we randomly vary the scaled magnetic field components, our initial guesses for *Dst1*, *Dst2*, *Dst3*, the speed (within the arrival speed error), and density along a normal distribution using 100,000 ensemble members. We also randomly vary the time shift ± 0.9 hours, which corresponds to the predicted arrival time error. The random temporal shift also takes into account the different arrival times of the CMEs. Figures 7a–d show the mapped magnetic field data as well as our assumptions for speed and density with the shaded areas indicating 1σ uncertainties. The resulting *Dst* values for STEREO-A (blue) and L1 (orange) data are given in Figure 7e, which we can compare with the observed SYM-H (black) and SYM-H (gray) values in Figure 7g.

Table 4 summarizes our results quantitatively and gives a comparison between observed and modeled geomagnetic indices as derived from shifted STEREO-A beacon and L1 data.

Table 4. Comparison between observed and modeled geomagnetic indices. Observed *Dst* and SYM-H values are taken from low and high resolution OMNI datasets. The geomagnetic indices are modeled from mapped STEREO-A beacon data as well as L1 data using the TL model. The error represents the 1σ uncertainty resulting from the ensemble.

Spacecraft	Time min(<i>Dst</i>) [UT]	Δt [h]	min(<i>Dst</i>) [nT]	Δ min(<i>Dst</i>) [nT]	RMSE(<i>Dst</i>) [nT]
OMNI	2024-05-11 02:00	–	–412.0	–	–
STEREO-A	2024-05-10 22:29	–3.5	-459.9 ± 54.8	-47.9 ± 55.4	152.3 ± 17.9
L1	2024-05-10 23:00	–3.2	–410.2	1.8	71.2
Spacecraft	Time min(<i>Dst</i>) [UT]	Δt [h]	min(<i>Dst</i>) [nT]	Δ min(<i>Dst</i>) [nT]	RMSE(<i>Dst</i>) [nT]
OMNI	2024-05-11 02:14	–	–518.0	–	–
STEREO-A	2024-05-10 21:13	–5.0	-478.5 ± 7.5	39.5 ± 9.7	171.5 ± 1.9
L1	2024-05-10 21:53	–4.3	–421.5	96.5	94.9

As can be seen in Figure 7h, the largest differences between calculated and observed SYM-H values occur on 10 May at 21:13 UT, where the minimum SYM-H value from STEREO-A data is predicted 5.0 hours too early. It is noteworthy that the minimum *Dst* and SYM-H values are also predicted too early by several hours when applying the TL model to L1 data. The minimum in B_z , associated with D2 as discussed in section 4, occurs at approximately the same time as the predicted SYM-H minimum from L1 data on 10 May 21:53 UT. This B_z minimum therefore appears to be an important driver for the TL model. However, for the observed SYM-H, the prolonged period of B_z after D3, which starts at 00:02 UT on 11 May, also appears to be a major contributor to the measured geomagnetic response. The actual SYM-H minimum is hence measured on 11 May 02:14 UT, whereas the model already predicts a recovery phase for indices derived from L1 and STEREO-A data. This leads to a rather high RMSE of 171.5 nT between STEREO-

A and observed SYM-H values. The RMSE is calculated for the duration of the event only, where the duration is indicated by the vertical bars in Figure 7. Unsurprisingly, the observed Dst and SYM-H values are better reproduced from L1 data, with RMSE = 71.2 nT and RMSE = 94.9 nT, respectively. However, due to the timing offset between calculated and modeled minimum Dst and SYM-H, the error is still large. When comparing the outcome from STEREO-A to SYM-H values derived using the L1 data, we calculate a RMSE of 39.2 nT, which is considerably lower than the RMSE of 171.5 nT calculated when comparing the STEREO-A SYM-H values to the observed OMNI SYM-H values. We therefore conclude that the model output is similar using either STEREO-A or L1 data, where the minima of the calculated geomagnetic indices are predicted earlier than the observed minima.

The observed minimum Dst index = -412.0 nT is well reproduced by the L1 data, $Dst_{L1} = -410.2$ nT, while the measured minimum of SYM-H = -518.0 nT is underestimated by 23%. Interestingly, the latter is also not resolved by the measured and hourly sampled Dst index. The fact that the minimum Dst value is better reproduced than the minimum SYM-H value is probably due to the bias we introduce when applying the TL model to 1-minute resolution data. The minimum Dst value from STEREO-A data, on the other hand, overestimates the minimum intensity of the geomagnetic storm by 47.9 nT and underestimates the observed minimum SYM-H value by 39.5 nT, with the modeled minimum Dst and SYM-H values being -459.9 nT and -478.5 nT, respectively.

6 Conclusions

In this study, we have investigated the geomagnetic superstorm which occurred on 10–12 May 2024 and was measured by ACE and STEREO-A, among other spacecraft. The fortunate position of the STEREO-A spacecraft, 12.6 degrees away from the Sun-Earth line and 0.05 AU closer to the Sun resulted in an observation of the event two hours and 34 minutes earlier than at L1. The event consisted of five solar coronal mass ejections, launched from the Sun between 8–9 May 2024, that drove the main geomagnetic activity. This analysis gives unprecedented insights into how forecasting of highly interactive geomagnetic superstorms may work with future potential missions.

First, we give an overview of the event, where we analyze the source and in situ signatures at L1 separately and then explore their connection to better understand the cause for the high geomagnetic response. We are able to identify the source regions of the CMEs that cause the superstorm and the proxies thereof allow us to derive the handedness of the CMEs. With the CMEs from the northern (southern) hemisphere having negative (positive) helicity, they seem to follow the hemispheric polarity rule (Pevtsov & Balasubramaniam, 2003). This also allows us to match the CMEs to their interplanetary counterparts as measured at L1 and STEREO-A. Furthermore, we model the propagation of the CMEs with the ELiptical Evolution model (ELEvo), which reproduces the arrival of the first CME at L1 well, with the difference between predicted and actual arrival being only 2 min, with a model error window of ± 7 hours. In contrast, the arrival at STEREO-A is predicted 1 hour and 34 min too early. With the successive launch of these five CMEs within 28 hours, expansion of the individual CMEs seems to be inhibited, which results in a preservation of high magnetic fields strengths at L1. Interestingly, however, the CMEs have yet not fully merged at L1 and individual magnetic ejecta can still be recognized in the magnetic field data of STEREO-A and L1. We have also identified discontinuities in the in situ data at L1 that appear to amplify B_z and hence make an important contribution to the geomagnetic response. These B_z minima could be the result of compressions possibly associated with CME-driven shocks propagating into the magnetic ejecta of the previous CMEs. Such shocks inside CMEs are frequent drivers of extreme B_z and hence geomagnetic effects (e.g. Liu et al., 2014; Lugaz et al., 2016; Scolini et al., 2020).

For modeling the geomagnetic effect from STEREO-A data we only use data available at the time of the event, as we want to reproduce a real-time scenario. We therefore have to estimate the plasma parameters, density and speed, that are not available in real-time. The STEREO-A beacon data are then shifted temporally and spatially to L1 to determine the accuracy with which the strength of the geomagnetic superstorm could have been forecasted 2.57 hours earlier from a sub-L1 position. To this end, we apply the Temerin and Li (2006) model to the mapped STEREO-A beacon data and compare the outcome to the observed Dst and SYM-H values. The predicted Dst and SYM-H minimum values of -459.9 ± 54.8 nT and -478.5 ± 7.5 nT, respectively, overestimate the observed minimum Dst index of -412 nT by 11% and underestimate the observed SYM-H of -518 nT by 8%. By also comparing these results calculated using STEREO-A data with the SYM-H values calculated from solar wind values measured at L1, we can isolate modeling effects from observational ones. We get an RMS error between the calculated SYM-H values from STEREO-A and L1 of 39.2 nT. When compared to the observed SYM-H values as given in the OMNI data, we get a comparatively high RMS error of 171.5 nT. The large RMSE most probably results from the minimum Dst (SYM-H) value being forecasted 3.5 (5.0) hours earlier than the observed minimum, which also leads to an early onset of the recovery phase. Since this is also the case for the Dst and SYM-H values derived from L1 data, we argue that the temporal difference in the minima between model and observation is probably due to the TL model itself, while the difference in the actual strength of the geomagnetic impact is an observational effect, with the magnetic field strengths at STEREO-A being higher still.

In comparison, by combining the empirical methods from Burton et al. (1975) and O'Brien and McPherron (2000), the authors of Liu et al. (2024) are able to reproduce the time of minimum Dst index for this event better than the TL model. In this post-analysis, the authors also model the Dst index of the May 2024 superstorm based on STEREO-A magnetic field data, but instead of estimating the missing plasma values, they use the density and solar wind speed as measured by the spacecraft *Wind*. The minimum Dst index calculated using L1 solar wind input in this paper is 8% lower than the actual minimum and amounts to -378 nT. In contrast, the minimum Dst index derived using STEREO-A data is -494 nT. The authors argue that the inferred geomagnetic indices from STEREO-A data give a lower limit, since the CMEs are more directed towards STEREO-A, possibly resulting in higher speeds and therefore even lower Dst values there. We agree that the actual geomagnetic impact at STEREO-A should have been higher than our inferred Dst of -459.9 nT, especially since our rough estimation of the density underestimates the measured mean density at L1 by 54%.

To summarize, we believe that this case study may represent a worst-case scenario for assessing the feasibility of future sub-L1 missions. The longitudinal distance between STEREO-A and L1 is at the outer range of what is recommended for sub-L1 missions, and the interaction of the five CMEs is both time- and space-dependent, with the time dependence being most evident in the dynamical evolution of D2. Despite these challenges, the prediction at STEREO-A is still acceptable compared to L1. Quantitatively, especially the period with SYM-H < -200 nT is predicted to be 21 h and 6 min, which agrees well with the measured duration of 23 h and 2 min. In addition, the overall correlation between modeled and observed geomagnetic indices is very good with a Pearson coefficient of 0.97. Probably not least because the RMSE between the B_z component measured by STEREO-A and L1 is small and amounts to 26.7 nT, with B_z being the most important parameter for the TL model. With our simple estimates, we would have been able to fairly accurately infer the strength of the geomagnetic storm 2.57 hours before its measurement at L1. This demonstrates the potential of future sub-L1 missions, especially since strongly interacting events, which are considered to be the main drivers of superstorms, cannot yet be reliably predicted otherwise.

Open Research Section

The data files used in this study and the animations that we produced can be found on figshare: <https://doi.org/10.6084/m9.figshare.27792873>. The code for creating the paper figures and results is available at https://github.com/EvaWeiler/may_2024_superstorm. The spacecraft data used in this study were obtained from these sources: STEREO-A beacon data were downloaded from the STEREO science center: <https://stereo-ssc.nascom.nasa.gov/data/beacon/ahead/impact/>. The ACE data are taken from the NOAA real time solar wind data product: <https://services.swpc.noaa.gov/products/solar-wind/>. The OMNI dataset provides the geomagnetic storm time (*Dst*) index and was obtained from https://spdf.gsfc.nasa.gov/pub/data/omni/low_res_omni/ (Papitashvili & King, 2020b), and the SYM-H index was downloaded from https://spdf.gsfc.nasa.gov/pub/data/omni/high_res_omni/ (Papitashvili & King, 2020a). This research used version 6.0.2 (<https://zenodo.org/records/13743565>) of the SunPy open source software package (SunPy Community et al., 2020). This work made use of Astropy: <http://www.astropy.org>, a community-developed core Python package and an ecosystem of tools and resources for astronomy (Astropy Collaboration et al., 2022).

Acknowledgments

E. W., C. M., E. D., U. A., and H. R. are funded by the European Union (ERC, HELIO4CAST, 101042188). Views and opinions expressed are however those of the author(s) only and do not necessarily reflect those of the European Union or the European Research Council Executive Agency. Neither the European Union nor the granting authority can be held responsible for them. We acknowledge the Community Coordinated Modeling Center (CCMC) at Goddard Space Flight Center for the use of the Space Weather Database Of Notifications, Knowledge, Information (DONKI), <https://kauai.ccmc.gsfc.nasa.gov/DONKI/>. N. L. acknowledges funding from 80NSSC24K1245 and 80NSSC20K0431. T. A., J. L. and M. B. acknowledge that this research was funded in whole, or in part, by the Austrian Science Fund (FWF) [P 36093]. S. M. and M. R. acknowledge that this research was funded in whole, or in part, by the Austrian Science Fund (FWF) [P 34437]. For the purpose of open access, the author has applied a CC BY public copyright licence to any Author Accepted Manuscript version arising from this submission.

References

- Abraham-Shrauner, B. (1972). Determination of magnetohydrodynamic shock normals. *Journal of Geophysical Research (1896-1977)*, 77(4), 736-739. Retrieved from <https://agupubs.onlinelibrary.wiley.com/doi/abs/10.1029/JA077i004p00736> doi: <https://doi.org/10.1029/JA077i004p00736>
- Abraham-Shrauner, B., & Yun, S. H. (1976). Interplanetary shocks seen by ames plasma probe on pioneer 6 and 7. *Journal of Geophysical Research (1896-1977)*, 81(13), 2097-2102. Retrieved from <https://agupubs.onlinelibrary.wiley.com/doi/abs/10.1029/JA081i013p02097> doi: <https://doi.org/10.1029/JA081i013p02097>
- Acuña, M. H., Curtis, D., Scheifele, J. L., Russell, C. T., Schroeder, P., Szabo, A., & Luhmann, J. G. (2008, April). The STEREO/IMPACT Magnetic Field Experiment. *Space Sci. Rev.*, 136(1-4), 203-226. doi: 10.1007/s11214-007-9259-2
- Astropy Collaboration, Price-Whelan, A. M., Lim, P. L., Earl, N., Starkman, N., Bradley, L., ... Astropy Project Contributors (2022, August). The Astropy Project: Sustaining and Growing a Community-oriented Open-source Project and the Latest Major Release (v5.0) of the Core Package. *Astrophys. J.*, 935(2), 167. doi: 10.3847/1538-4357/ac7c74
- Borovsky, J. E. (2018). The spatial structure of the oncoming solar wind at earth and the shortcomings of a solar-wind monitor at l1. *Journal of Atmospheric and Solar-Terrestrial Physics*, 177, 2-11. Retrieved from <https://>

- www.sciencedirect.com/science/article/pii/S1364682617300159 (Dynamics of the Sun-Earth System: Recent Observations and Predictions) doi: <https://doi.org/10.1016/j.jastp.2017.03.014>
- Bothmer, V., & Schwenn, R. (1998, January). The structure and origin of magnetic clouds in the solar wind. *Ann. Geophys.*, *16*, 1-24. doi: 10.1007/s00585-997-0001-x
- Brueckner, G. E., Howard, R. A., Koomen, M. J., Korendyke, C. M., Michels, D. J., Moses, J. D., ... Eyles, C. J. (1995, December). The Large Angle Spectroscopic Coronagraph (LASCO). *Solar Phys.*, *162*, 357-402. doi: 10.1007/BF00733434
- Burt, J., & Smith, B. (2012). Deep space climate observatory: The dscovr mission. In *2012 ieee aerospace conference* (p. 1-13). doi: 10.1109/AERO.2012.6187025
- Burton, R. K., McPherron, R. L., & Russell, C. T. (1975). An empirical relationship between interplanetary conditions and dst. *Journal of Geophysical Research (1896-1977)*, *80*(31), 4204-4214. Retrieved from <https://agupubs.onlinelibrary.wiley.com/doi/abs/10.1029/JA080i031p04204> doi: <https://doi.org/10.1029/JA080i031p04204>
- Chen, P. F., Harra, L. K., & Fang, C. (2014, March). Imaging and Spectroscopic Observations of a Filament Channel and the Implications for the Nature of Counter-streamings. *Astrophys. J.*, *784*(1), 50. doi: 10.1088/0004-637X/784/1/50
- Colburn, D. S., & Sonett, C. P. (1966, June). Discontinuities in the Solar Wind. *Space Sci. Rev.*, *5*(4), 439-506. doi: 10.1007/BF00240575
- Collado Villaverde, A., Muñoz, P., & Cid, C. (2023, 10). Classifying and bounding geomagnetic storms based on the sym-h and asy-h indices. *Natural Hazards*, *120*, 1-22. doi: 10.1007/s11069-023-06241-1
- Cyr, O. C. S., Mesarch, M. A., Maldonado, H. M., Folta, D. C., Harper, A. D., Davila, J. M., & Fisher, R. R. (2000, September). Space Weather Diamond: a four spacecraft monitoring system. *Journal of Atmospheric and Solar-Terrestrial Physics*, *62*(14), 1251-1255. doi: 10.1016/S1364-6826(00)00069-9
- Davies, E. E., Forsyth, R. J., Winslow, R. M., Möstl, C., & Lugaz, N. (2021, December). A Catalog of Interplanetary Coronal Mass Ejections Observed by Juno between 1 and 5.4 au. *Astrophys. J.*, *923*(2), 136. doi: 10.3847/1538-4357/ac2ccb
- Domingo, V., Fleck, B., & Poland, A. I. (1995, December). The SOHO Mission: an Overview. *Solar Phys.*, *162*(1-2), 1-37. doi: 10.1007/BF00733425
- Eastwood, J. P., Kataria, D. O., McInnes, C. R., Barnes, N. C., & Mulligan, P. (2015, January). Sunjammer. *Weather*, *70*(1), 27-30. doi: 10.1002/wea.2438
- Eyles, C. J., Harrison, R. A., Davis, C. J., Waltham, N. R., Shaughnessy, B. M., Mapson-Menard, H. C. A., ... others (2009, February). The Heliospheric Imagers Onboard the STEREO Mission. *Solar Phys.*, *254*(2), 387-445. doi: 10.1007/s11207-008-9299-0
- Good, S. W., & Forsyth, R. J. (2016, January). Interplanetary Coronal Mass Ejections Observed by MESSENGER and Venus Express. *Solar Phys.*, *291*(1), 239-263. doi: 10.1007/s11207-015-0828-3
- Hapgood, M. A. (1992, May). Space physics coordinate transformations: A user guide. *Planet. Space Sci.*, *40*(5), 711-717. doi: 10.1016/0032-0633(92)90012-D
- Harvey, J. W., Hill, F., Hubbard, R. P., Kennedy, J. R., Leibacher, J. W., Pintar, J. A., ... Yasukawa, E. (1996, May). The Global Oscillation Network Group (GONG) Project. *Science*, *272*(5266), 1284-1286. doi: 10.1126/science.272.5266.1284
- Hayakawa, H., Ebihara, Y., Mishev, A., Koldobskiy, S., Kusano, K., Bechet, S., ... Miyoshi, Y. (2024, 07). *The solar and geomagnetic storms in may 2024: A*

- flash data report*. doi: 10.48550/arXiv.2407.07665
- Henon, M. (1969, February). Numerical exploration of the restricted problem, V. *Astron. Astrophys.*, *1*, 223-238.
- Jarolim, R., Veronig, A., Purkhart, S., Zhang, P., & Rempel, M. (2024, September). Magnetic Field Evolution of the Solar Active Region 13664. *arXiv e-prints*, arXiv:2409.08124. doi: 10.48550/arXiv.2409.08124
- Ji, E.-Y., Moon, Y.-J., Gopalswamy, N., & Lee, D.-H. (2012). Comparison of dst forecast models for intense geomagnetic storms. *Journal of Geophysical Research: Space Physics*, *117*(A3). Retrieved from <https://agupubs.onlinelibrary.wiley.com/doi/abs/10.1029/2011JA016872> doi: <https://doi.org/10.1029/2011JA016872>
- Kaiser, M. L., Kucera, T. A., Davila, J. M., St. Cyr, O. C., Guhathakurta, M., & Christian, E. (2008, April). The STEREO Mission: An Introduction. *Space Sci. Rev.*, *136*(1-4), 5-16. doi: 10.1007/s11214-007-9277-0
- Kilpua, E., Lugaz, N., Mays, M. L., & Temmer, M. (2019). Forecasting the structure and orientation of earthbound coronal mass ejections. *Space Weather*, *17*(4), 498-526. Retrieved from <https://agupubs.onlinelibrary.wiley.com/doi/abs/10.1029/2018SW001944> doi: <https://doi.org/10.1029/2018SW001944>
- Koehn, G. J., Desai, R. T., Davies, E. E., Forsyth, R. J., Eastwood, J. P., & Poedts, S. (2022, dec). Successive interacting coronal mass ejections: How to create a perfect storm. *The Astrophysical Journal*, *941*(2), 139. Retrieved from <https://dx.doi.org/10.3847/1538-4357/aca28c> doi: 10.3847/1538-4357/aca28c
- Kubicka, M., Möstl, C., Amerstorfer, T., Boakes, P. D., Feng, L., Eastwood, J. P., & Törmänen, O. (2016, December). Prediction of Geomagnetic Storm Strength from Inner Heliospheric In Situ Observations. *Astrophys. J.*, *833*(2), 255. doi: 10.3847/1538-4357/833/2/255
- Laker, R., Horbury, T. S., O'Brien, H., Fauchon-Jones, E. J., Angelini, V., Fargette, N., ... Dumbović, M. (2024, February). Using Solar Orbiter as an Upstream Solar Wind Monitor for Real Time Space Weather Predictions. *Space Weather*, *22*(2), e2023SW003628. doi: 10.1029/2023SW003628
- Lemen, J. R., Title, A. M., Akin, D. J., Boerner, P. F., Chou, C., Drake, J. F., ... others (2012, January). The Atmospheric Imaging Assembly (AIA) on the Solar Dynamics Observatory (SDO). *Solar Phys.*, *275*(1-2), 17-40. doi: 10.1007/s11207-011-9776-8
- Lindsay, G. M., Russell, C. T., & Luhmann, J. G. (1999, May). Predictability of Dst index based upon solar wind conditions monitored inside 1 AU. *J. Geophys. Res.*, *104*(A5), 10335-10344. doi: 10.1029/1999JA900010
- Liu, Y. D., Hu, H., Zhao, X., Chen, C., & Wang, R. (2024). *A pileup of coronal mass ejections produced the largest geomagnetic storm in two decades*. Retrieved from <https://arxiv.org/abs/2409.11492>
- Liu, Y. D., Luhmann, J. G., Kajdič, P., Kilpua, E. K. J., Lugaz, N., Nitta, N. V., ... others (2014, March). Observations of an extreme storm in interplanetary space caused by successive coronal mass ejections. *Nat. Commun.*, *5*, 3481. doi: 10.1038/ncomms4481
- Love, J. J., Rigler, E. J., Hayakawa, H., & Mursula, K. (2024, August). On the uncertain intensity estimate of the 1859 Carrington storm. *Journal of Space Weather and Space Climate*, *14*, 21. doi: 10.1051/swsc/2024015
- Love, J. J., Rigler, E. J., Pulkkinen, A., & Riley, P. (2015, August). On the log-normality of historical magnetic storm intensity statistics: Implications for extreme-event probabilities. *Geophys. Res. Lett.*, *42*(16), 6544-6553. doi: 10.1002/2015GL064842
- Lugaz, N., Farrugia, C. J., Winslow, R. M., Al-Haddad, N., Kilpua, E. K. J., & Riley, P. (2016). Factors affecting the geoeffectiveness of shocks and sheaths at 1 au. *Journal of Geophysical Research: Space Physics*, *121*(11), 10,861-

- 10,879. Retrieved from <https://agupubs.onlinelibrary.wiley.com/doi/abs/10.1002/2016JA023100> doi: <https://doi.org/10.1002/2016JA023100>
- Lugaz, N., IV, W. B. M., & Gombosi, T. I. (2005, nov). Numerical simulation of the interaction of two coronal mass ejections from sun to earth. *The Astrophysical Journal*, *634*(1), 651. Retrieved from <https://dx.doi.org/10.1086/491782> doi: 10.1086/491782
- Lugaz, N., Lee, C. O., Al-Haddad, N., Lillis, R. J., Jian, L. K., Curtis, D. W., ... Nieves-Chinchilla, T. (2024, Sep 20). The need for near-earth multi-spacecraft heliospheric measurements and an explorer mission to investigate interplanetary structures and transients in the near-earth heliosphere. *Space Science Reviews*, *220*(7), 73. Retrieved from <https://doi.org/10.1007/s11214-024-01108-8> doi: 10.1007/s11214-024-01108-8
- Lugaz, N., Zhuang, B., Scolini, C., Al-Haddad, N., Farrugia, C. J., Winslow, R. M., ... Galvin, A. B. (2024, feb). The width of magnetic ejecta measured near 1 au: Lessons from stereo-a measurements in 2021–2022. *The Astrophysical Journal*, *962*(2), 193. Retrieved from <https://dx.doi.org/10.3847/1538-4357/ad17b9> doi: 10.3847/1538-4357/ad17b9
- Mac Manus, D. H., Rodger, C. J., Renton, A., Ronald, J., Harper, D., Taylor, C., ... Clilverd, M. A. (2023). Geomagnetically induced current mitigation in new zealand: Operational mitigation method development with industry input. *Space Weather*, *21*(11), e2023SW003533. Retrieved from <https://agupubs.onlinelibrary.wiley.com/doi/abs/10.1029/2023SW003533> (e2023SW003533 2023SW003533) doi: <https://doi.org/10.1029/2023SW003533>
- Martin, S. F. (1998, September). Conditions for the Formation and Maintenance of Filaments (Invited Review). *Solar Phys.*, *182*(1), 107-137. doi: 10.1023/A:1005026814076
- McComas, D. J., Bame, S. J., Barker, P., Feldman, W. C., Phillips, J. L., Riley, P., & Griffiee, J. W. (1998, July). Solar Wind Electron Proton Alpha Monitor (SWEPAM) for the Advanced Composition Explorer. *Space Sci. Rev.*, *86*, 563-612. doi: 10.1023/A:1005040232597
- Meng, X., Tsurutani, B. T., & Mannucci, A. J. (2019, June). The Solar and Interplanetary Causes of Superstorms (Minimum Dst \leq -250 nT) During the Space Age. *Journal of Geophysical Research (Space Physics)*, *124*(6), 3926-3948. doi: 10.1029/2018JA026425
- Morley, S. K. (2020). Challenges and opportunities in magnetospheric space weather prediction. *Space Weather*, *18*(3), e2018SW002108. Retrieved from <https://agupubs.onlinelibrary.wiley.com/doi/abs/10.1029/2018SW002108> (e2018SW002108 10.1029/2018SW002108) doi: <https://doi.org/10.1029/2018SW002108>
- Möstl, C., Rollett, T., Frahm, R. A., Liu, Y. D., Long, D. M., Colaninno, R. C., ... Vršnak, B. (2015, May). Strong coronal channelling and interplanetary evolution of a solar storm up to Earth and Mars. *Nature Communications*, *6*, 7135. doi: 10.1038/ncomms8135
- Möstl, C., Weiss, A., Bailey, R., & Reiss, M. (2020, Jun). *Helcats interplanetary coronal mass ejection catalog v2.0*. figshare. Retrieved from https://figshare.com/articles/dataset/HELCASTS_Interplanetary_Coronal_Mass_Ejection_Catalog_v2.0/6356420/7 doi: 10.6084/m9.figshare.6356420.v7
- Nose, M., Iyemori, T., Sugiura, M., & Kamei, T. (2015). *Geomagnetic dst index*. World Data Center for Geomagnetism, Kyoto. Retrieved from https://isds-datadoi.nict.go.jp/wds/10.17593_14515-74000.html doi: 10.17593/14515-74000
- O'Brien, T., & McPherron, R. L. (2000). Forecasting the ring current index dst in real time. *Journal of Atmospheric and Solar-Terrestrial Physics*, *62*(14), 1295-1299. Retrieved from <https://www.sciencedirect.com/science/article/>

- pii/S1364682600000729 (Space Weather Week) doi: [https://doi.org/10.1016/S1364-6826\(00\)00072-9](https://doi.org/10.1016/S1364-6826(00)00072-9)
- Palmerio, E., Kilpua, E. K. J., James, A. W., Green, L. M., Pomoell, J., Isavnin, A., & Valori, G. (2017, February). Determining the Intrinsic CME Flux Rope Type Using Remote-sensing Solar Disk Observations. *Solar Phys.*, *292*(2), 39. doi: 10.1007/s11207-017-1063-x
- Papitashvili, N. E., & King, J. H. (2020a). *Omni 1-min data*. NASA Space Physics Data Facility. doi: 10.48322/45bb-8792
- Papitashvili, N. E., & King, J. H. (2020b). *Omni hourly data*. NASA Space Physics Data Facility. doi: 10.48322/1shr-ht18
- Pesnell, W. D., Thompson, B. J., & Chamberlin, P. C. (2012, January). The Solar Dynamics Observatory (SDO). *Solar Phys.*, *275*(1-2), 3-15. doi: 10.1007/s11207-011-9841-3
- Pevtsov, A. A., & Balasubramaniam, K. S. (2003, January). Helicity patterns on the sun. *Advances in Space Research*, *32*(10), 1867-1874. doi: 10.1016/S0273-1177(03)90620-X
- Riley, P. (2012, February). On the probability of occurrence of extreme space weather events. *Space Weather*, *10*(2), 02012. doi: 10.1029/2011SW000734
- Ritter, B., Meskers, A. J. H., Miles, O., Rußwurm, M., Scully, S., Roldán, A., ... Ruffenach, A. (2015, February). A Space Weather Information Service Based Upon Remote and In-Situ Measurements of Coronal Mass Ejections Heading for Earth. *Journ. Space Weather Space Climate*, *5*. doi: 10.1051/swsc/2015006
- Scherrer, P. H., Schou, J., Bush, R. I., Kosovichev, A. G., Bogart, R. S., Hoeksema, J. T., ... Tomczyk, S. (2012, January). The Helioseismic and Magnetic Imager (HMI) Investigation for the Solar Dynamics Observatory (SDO). *Solar Phys.*, *275*(1-2), 207-227. doi: 10.1007/s11207-011-9834-2
- Schwartz, S. J. (1998, January). Shock and Discontinuity Normals, Mach Numbers, and Related Parameters. *ISSI Scientific Reports Series*, *1*, 249-270.
- Scolini, C., Chané, E., Temmer, M., Kilpua, E. K. J., Dissauer, K., Veronig, A. M., ... Poedts, S. (2020, feb). Cme-cme interactions as sources of cme geoeffectiveness: The formation of the complex ejecta and intense geomagnetic storm in 2017 early september. *The Astrophysical Journal Supplement Series*, *247*(1), 21. Retrieved from <https://dx.doi.org/10.3847/1538-4365/ab6216> doi: 10.3847/1538-4365/ab6216
- Smith, C. W., L'Heureux, J., Ness, N. F., Acuña, M. H., Burlaga, L. F., & Scheifele, J. (1998, July). The ACE Magnetic Fields Experiment. *Space Sci. Rev.*, *86*, 613-632. doi: 10.1023/A:1005092216668
- Spogli, L., Alberti, T., Bagiacchi, P., cafarella, I., Cesaroni, C., Cianchini, G., ... viola, m. (2024, 06). The effects of the may 2024 mother's day superstorm over the mediterranean sector: from data to public communication. *Annals of geophysics = Annali di geofisica*, *67*, 218. doi: 10.4401/ag-9117
- Stone, E. C., Frandsen, A. M., Mewaldt, R. A., Christian, E. R., Margolies, D., Ormes, J. F., & Snow, F. (1998, July). The Advanced Composition Explorer. *Space Sci. Rev.*, *86*, 1-22. doi: 10.1023/A:1005082526237
- Sugiura, M. (1964). Hourly values of equatorial dst for the igy. *Annals of the International Geophysical Year*.
- SunPy Community, Barnes, W. T., Bobra, M. G., Christe, S. D., Freij, N., Hayes, L. A., ... Dang, T. K. (2020, February). The SunPy Project: Open Source Development and Status of the Version 1.0 Core Package. *Astrophys. J.*, *890*(1), 68. doi: 10.3847/1538-4357/ab4f7a
- Temerin, M., & Li, X. (2006, April). Dst model for 1995-2002. *J. Geophys. Res.(Space Physics)*, *111*(A4), A04221. doi: 10.1029/2005JA011257
- Temmer, M., Scolini, C., Richardson, I. G., Heinemann, S. G., Paouris, E., Vourlidas, A., ... Zhuang, B. (2023). Cme propagation through the heliosphere: Sta-

- tus and future of observations and model development. *Advances in Space Research*. Retrieved from <https://www.sciencedirect.com/science/article/pii/S0273117723005239> doi: <https://doi.org/10.1016/j.asr.2023.07.003>
- Themens, D. R., Elvidge, S., McCaffrey, A., Jayachandran, P. T., Coster, A., Varney, R. H., ... Reid, B. (2024). The high latitude ionospheric response to the major may 2024 geomagnetic storm: A synoptic view. *Geophysical Research Letters*, *51*(19), e2024GL111677. Retrieved from <https://agupubs.onlinelibrary.wiley.com/doi/abs/10.1029/2024GL111677> (e2024GL111677 2024GL111677) doi: <https://doi.org/10.1029/2024GL111677>
- Vourlidis, A., Patsourakos, S., & Savani, N. P. (2019, July). Predicting the geoeffective properties of coronal mass ejections: current status, open issues and path forward. *Philosophical Transactions of the Royal Society of London Series A*, *377*(2148), 20180096. doi: 10.1098/rsta.2018.0096
- Vršnak, B., Žic, T., Vrbanec, D., Temmer, M., Rollett, T., Möstl, C., ... Shanmugaraju, A. (2013, Jul). Propagation of Interplanetary Coronal Mass Ejections: The Drag-Based Model. *Solar Phys.*, *285*(1-2), 295-315. doi: 10.1007/s11207-012-0035-4
- Wang, R., Liu, Y. D., Zhao, X., & Hu, H. (2024). *Unveiling key factors in the solar eruptions leading to the solar superstorm in 2024 may*. Retrieved from <https://arxiv.org/abs/2410.00891>
- Wanliss, J. A., & Showalter, K. M. (2006). High-resolution global storm index: Dst versus sym-h. *Journal of Geophysical Research: Space Physics*, *111*(A2). Retrieved from <https://agupubs.onlinelibrary.wiley.com/doi/abs/10.1029/2005JA011034> doi: <https://doi.org/10.1029/2005JA011034>
- Weiss, A. J., Möstl, C., Amerstorfer, T., Bailey, R. L., Reiss, M. A., Hinterreiter, J., ... Bauer, M. (2021, January). Analysis of Coronal Mass Ejection Flux Rope Signatures Using 3DCORE and Approximate Bayesian Computation. *Astrophys. J. Suppl. S.*, *252*(1), 9. doi: 10.3847/1538-4365/abc9bd
- Weiss, A. J., Möstl, C., Davies, E. E., Amerstorfer, T., Bauer, M., Hinterreiter, J., ... Baumjohann, W. (2021, December). Multi-point analysis of coronal mass ejection flux ropes using combined data from Solar Orbiter, BepiColombo, and Wind. *Astron. Astrophys.*, *656*, A13. doi: 10.1051/0004-6361/202140919
- Zhang, J., Richardson, I. G., Webb, D. F., Gopalswamy, N., Huttunen, E., Kasper, J. C., ... Zhukov, A. N. (2007, October). Solar and interplanetary sources of major geomagnetic storms (Dst \leq -100 nT) during 1996-2005. *Journal of Geophysical Research (Space Physics)*, *112*(A10), A10102. doi: 10.1029/2007JA012321
- Čalogović, J., Dumbović, M., Sudar, D., Vršnak, B., Martinić, K., Temmer, M., & Veronig, A. M. (2021, July). Probabilistic drag-based ensemble model (dbem) evaluation for heliospheric propagation of cmes. *Solar Physics*, *296*(7). Retrieved from <http://dx.doi.org/10.1007/s11207-021-01859-5> doi: 10.1007/s11207-021-01859-5